



Canard-Wing Interference Effects on the Flight Characteristics of a Transonic Passenger Aircraft

Sean Harrison*, Ryan Darragh†, Peter E. Hamlington‡

*Turbulence and Energy Systems Laboratory, Department of Mechanical Engineering,
 University of Colorado, Boulder, Colorado 80309, United States*

Mehdi Ghoreyshi§ and Andrew J. Lofthouse¶

*High Performance Computing Research Center, U.S. Air Force Academy
 USAF Academy, Colorado 80840, United States*

Effects of canard wing interference on the flight characteristics of a civilian transonic cruiser are examined. The aircraft is an unconventional design concept with no historical data. The flight characteristics of the aircraft are predicted using aerodynamic models in the form of look-up tables, generated using high-fidelity computational fluid dynamics simulations and a potential flow solver. These tables contain longitudinal and lateral force and moment coefficients for different combinations of angle of attack, side-slip angle, and control surface deflections. Dynamic damping derivatives are calculated from time-accurate simulations of the aircraft models oscillating in pitch, roll, and yaw direction and using a linear regression estimation method. The static simulations are performed at a Mach number of 0.117, as reported in wind tunnel experiments, and for two different canard positions using an overset grid approach. The aerodynamic tables include canard deflections of $[-30^\circ, -10^\circ, 0, 10^\circ]$ at angles of attack from -4° to 30° . Lateral coefficients are simulated at sideslip angles of -6° and 6° as well. The dynamic simulations are performed for aircraft oscillations about mean angles of attack between zero to ten degrees with a motion frequency of 1Hz and amplitude of 0.5 degrees. The predicted aerodynamic data are then compared with those measured in wind tunnel experiments and calculated from the potential flow solver. The results show that both static and dynamic predictions match reasonably well with experiments for the range of angles considered. The comparison plots show that the potential flow solver cannot predict the vortical flows formed over the wing and canard surfaces and thus the breaks seen in the experimental pitching moments. The potential flow solver predicts nearly linear aerodynamic data. The predicted dynamic damping derivatives from the potential solver do not match the experimental data due to not having the fuselage section in the model and inability of the solver to predict vortical flows over the vehicle. The aerodynamic models are then used in a stability and control analysis code to investigate the trim setting and handling quality of different canard designs. Overall, computed aerodynamics from the high-fidelity solver leads to similar flight dynamics results obtained from experimental data. The results show that positioning the canard surface of this vehicle closer to the wing requires less canard deflection and thrust force to trim the aircraft. These results confirm that computational fluid dynamics is a promising tool in design and flight dynamics investigation of aircraft with no historical data.

*Undergraduate Student, Mechanical Engineering, Sean.Harrison@colorado.edu

†Graduate Student, Aerospace Engineering Sciences, Ryan.Darragh@colorado.edu

‡Assistant Professor, Mechanical Engineering, Peter.Hamlington@colorado.edu, AIAA Member

§Senior Aerospace Engineer, Mehdi.Ghoreyshi@usafa.edu, AIAA Senior Member

¶Director, High Performance Computing Research Center, Andrew.Lofthouse@usafa.edu, AIAA Senior Member

Nomenclature

a	speed of sound, m/s
b	wing span, m
c	mean aerodynamic chord, m
f	frequency, Hz
C_D	drag coefficient, $D/q_\infty S$
C_L	lift coefficient, $L/q_\infty S$
C_N	normal-force coefficient, $N/q_\infty S$
C_m	pitching moment coefficient, $M_y/q_\infty S c$
C_p	pressure coefficient $(p - p_\infty)/q_\infty$
C_{ROLL}	rolling moment coefficient, $M_x/q_\infty S b$
C_{YAW}	yawing moment coefficient, $M_z/q_\infty S b$
C_Y	side-force coefficient $Y/q_\infty S$
D	drag force, N
D_v	fuselage vertical diameter, m
L	lift force, N
L_f	fuselage length, N
M	Mach number, V/a
PDF	pitch damping force, 1/rad
PDM	pitch damping moment, 1/rad
M_x, M_y, M_z	rolling, pitching, and yawing moments, N.m
p, q, r	roll, pitch, and yaw rates, rad/s
q_∞	dynamic pressure, Pa
RDM	roll damping moment, 1/rad
S_w	wing area, m^2
S_c	canard area, m^2
V	speed of aircraft, m/s
x, y, z	grid coordinates, m
x_c	canard apex position, m
YDM	yaw damping moment, 1/rad

Greek

α	angle of attack, deg or rad
β	side-slip angle, deg or rad
$\dot{\alpha}$	time-rate of change of angle of attack, rad/s
ϕ_c	canard deflection angle, deg
ρ	air density, kg/m^3
μ	air viscosity, $kg/(m.s)$
ω	angular velocity, rad/s
ω_{nd}	un-damped angular velocity, rad/s
θ	pitch angle, deg or rad
ζ_d	damping ratio

I. Introduction

Aircraft design is traditionally an expensive process that requires slow, costly, and potentially dangerous flight testing. Traditionally, aircraft conceptual design relies on aerodynamic models generated from previous experience and/or semi-empirical methods.^{1,2} These estimations are then used to find the stability and performance data and to size the control surfaces.³ These methods will likely lead to errors in sizing the control surfaces especially for unconventional configurations. To remedy any detected problem(s) in prototype testing, sometimes the whole design cycle needs to be repeated. This will significantly increase the aircraft production costs.

Computational fluid dynamics (CFD) provides a means by which to reduce these costs and provide enough accurate aerodynamic data to use in the design process. With recent advances in automated solid modeling and grid generation, it is now possible to rapidly create a parameterized watertight surface model of a concept aircraft. This modeling approach allows designers to screen different configurations prior to building the first prototype. This translates into an overall cost reduction and limiting risks. Specifically, the positioning of lift-producing surfaces such as canards can be manipulated to determine the effects of many different configurations on the flight characteristics of an aircraft. The effects of these lifting surfaces can easily be modeled in CFD for various deflection angles, positions, and sizes. These changes can all be implemented and analyzed computationally, thereby avoiding the need to build and test many different experimental models.

In the present study, the effects of different canard configurations on the flight characteristics of a transonic passenger aircraft concept is examined. This design concept, named the TransCRuiser (TCR), was proposed by the Swedish aerospace company SAAB and was studied using in-house design procedures at SAAB. Since then, the design has undergone several design changes including the addition of a front canard to improve the aircraft handling qualities in particular during a European project named SimSAC.⁴ The addition of a canard provides a secondary lifting surface that could make the aircraft stall-proof, since the canard will stall before the main wing. This induces a pitching moment on the aircraft, thus reducing its angle of attack until the canard begins to generate lift again.⁵ However, the canard also tends to reduce the stability of the aircraft when compared to conventional designs.

There is no historical data available to accurately predict the TCR aerodynamic data. The semi-empirical methods such as Digital DATCOM⁶ are limited to model the TCR with a canard as well. Ghoreyshi *et al.*⁵ detailed some flow features of TCR at different angles of attack and at low subsonic speeds. Both the wing and canard have rounded leading edges and are swept back above 50° that cause a complex vortex formation at moderate to high angles of attack. At about $\alpha = 12^\circ$, a canard vortex and an inboard and outboard wing vortex are present. The wing in the presence of the canard shows smaller inboard vortices than the canardless configuration; this is due to canard downwash effects that reduce the local angle of attack behind the canard span. On the other hand, the wing outboard vortex is slightly bigger in the presence of the canard. The canard vortex becomes larger with increasing angle of attack. At about $\alpha = 18^\circ$, the wing vortices merge. At about $\alpha = 20^\circ$, the canard vortex lifts up from the surface as well. At higher angles, the canard in the TCR aircraft has favorable effects on the wing aerodynamic performance. The wing behind the canard has a stronger merged vortex than the wing-only configuration which can delay the vortex breakdown. Note that these complex flow-fields cannot be predicted by a potential flow solver or a vortex lattice method.

Canard placement and surface area on the TCR has been investigated in Ref. 7, in which the primary concern was the flight dynamic investigation of the aircraft, as well as by Eliasson *et al.*,¹ whose concerns included the selection of the canard position. This study found that by positioning a canard closer to the nose of the aircraft, a smaller deflection was required to achieve trim because the canard has a bigger moment arm about the center of gravity. However, the aerodynamic data in this work were generated from a vortex lattice method (VLM) solver and the authors did not state whether the changes in aircraft's center of gravity with canard position have been taken into account as well.

Specifically, this paper investigates the effects of two different canard positions on flight characteristics of the TCR using high-fidelity computational methods. The first position examined is the recommended position specified by Eliasson *et al.*¹ In the second position, the canard is placed closer to the wing. Four different canard deflection angles are considered: $[-30^\circ, -10^\circ, 0, 10^\circ]$. The flight dynamics of both configurations were studied in the Computerized Environment for Aircraft Synthesis and Integrated Optimization Methods (CEASIOM) code.⁴ The code has aerodynamic, structure, propulsion, weight and balance, and stability and control modules. The aerodynamic models are in form of look-up tables. The aerodynamic sources available in the code are Digital DATCOM and a potential flow solver, Tornado. The aerodynamic tables from external flow solvers and wind tunnel experiments can be input to the code as well. In this work, the aerodynamic tables of TCR designs are generated by Cobalt flow solver, Tornado code, and from wind tunnel experiments. These tables are then used in the SDSA (stability and control module in CEASIOM) to investigate the flight characteristics of TCR aircraft.

There are two main objectives in the present study: 1) to compare the aircraft flight characteristics of the aircraft predicted from different aerodynamic sources, 2) and to investigate the effects of canard placements on the aircraft handling quality and trim settings. The paper is organized as follows. The next section reviews the computational methods. Next, the TCR geometry and grid details are provided. The results are

then presented and discussed, followed by concluding remarks.

II. Formulation

A. CEASIOM Aircraft Design Code

The CEASIOM code, used in this work, incorporates a parameterized description of the aircraft geometry. The geometry parameters include lifting surfaces, engines, control surfaces, and a fuselage. The lifting surfaces are defined using the apex position and placement, leading edge sweep angle, dihedral angle, span, wing area, taper ratio. The vertical tail can have a lateral displacement with a tilt angle as well. The strake is defined by span and leading edge sweep angle. A number of aircraft can be defined using this definition.

CEASIOM starts from these initial parameters and allows the design to be refined by adding winglet and cranked wings. In general, an aircraft geometry can be defined in CEASIOM with approximately 100 design variables. The code could generate a water-tight solid model of the design concept as well. Note that due to limitation of geometry parameters, the CEASIOM-generated models might have rough geometries at joints and junctions. However, Ghoreyshi *et al.*⁵ showed that these rough geometries do not affect the overall design trends obtained from viscous flow solvers.

B. Aerodynamic Tables

Aerodynamic models considered in this work are in the form of look-up tables. These tables are then used in an aircraft stability and control analysis code. The aerodynamic coefficients of TCR can be found as:

$$C_i = C_{i0}(\alpha, M, \beta) + C_{iq}(\alpha, M, q) \cdot \frac{cq}{2V} + C_{ip}(\alpha, M, p) \cdot \frac{bp}{2V} + C_{ir}(\alpha, M, r) \cdot \frac{br}{2V} + C_{i\phi_j}(\alpha, M, \delta) \cdot \phi_j \quad (1)$$

where $i = L, D, m, Y, ROLL, YAW$, representing lift, drag, pitching moment, side-force, rolling and yawing moment coefficients, respectively. $\phi_j = [\phi_c, \phi_a, \phi_r]$ includes canard, aileron, and rudder deflections, p, q, r are roll, pitch, and yaw rates. C_{iq}, C_{ip}, C_{ir} are damping derivatives as well. The coefficients in front of the aircraft states and control are named stability derivative which in general are functions of angle of attack, Mach number, and etc. These functions are represented in form of a look-up table as shown in Table 1.

Table 1. Aerodynamic database format, “x” indicates a column vector of non-zero elements.

α	M	β	ϕ_c	ϕ_r	ϕ_a	q	p	r	C_L	C_D	C_m	C_Y	C_{ROLL}	C_{YAW}
x	x	x	-	-	-	-	-	-	x	x	x	x	x	x
x	x	-	x	-	-	-	-	-	x	x	x	x	x	x
x	x	-	-	x	-	-	-	-	x	x	x	x	x	x
x	x	-	-	-	x	-	-	-	x	x	x	x	x	x
x	x	-	-	-	-	x	-	-	x	x	x	x	x	x
x	x	-	-	-	-	-	x	-	x	x	x	x	x	x
x	x	-	-	-	-	-	-	x	x	x	x	x	x	x

This table consists of seven sub-tables, each having three aerodynamic variables, where two variables are the angle of attack, α , and Mach number, M . For any given flight conditions, the aerodynamic coefficients can be interpolated from these sub-tables and the total coefficient then be found from Eq. 1. TCR aerodynamic tables are generated for Mach numbers of 0.117 and 0.9. The angle of attack ranges from -10° to 30° with two degrees increment. Side-slip angles include -6 and $+6$ degrees. Four different canard deflection angles are considered: $[-30^\circ, -10^\circ, 0, 10^\circ]$. Aileron and rudder deflections include $[-15^\circ$ and $15^\circ]$ as well. This results in a table with 576 entities.

C. Tornado Code

The vortex lattice solver, Tornado,⁸ can predict a wide range of aircraft stability and control aerodynamic derivatives using a vortex lattice approach. The code models various lifting surfaces such as wing, fin, and

canard. The fuselage is modeled by a thin plate. For control surface deflections, the vortex points located at the trailing edge of the flap are rotated around the hinge line which makes the wake change direction slightly.⁸ The version of the code used in this study does not model the fuselage and include some viscous corrections.

D. Cobalt Solver

Cobalt solves the unsteady, three-dimensional, compressible Navier-Stokes equations in an inertial reference frame. Arbitrary cell types in two or three dimensions may be used; a single grid therefore can be composed of different cell types.⁹ In Cobalt, the Navier-Stokes equations are discretized on arbitrary grid topologies using a cell-centered finite volume method. Second-order accuracy in space is achieved using the exact Riemann solver of Gottlieb and Groth,¹⁰ and least squares gradient calculations using QR factorization. To accelerate the solution of the discretized system, a point-implicit method using analytic first-order inviscid and viscous Jacobians is used. A Newtonian sub-iteration method is used to improve the time accuracy of the point-implicit method. Tomaro et al.¹¹ converted the code from explicit to implicit, enabling Courant-Friedrichs-Lewy (CFL) numbers as high as 10^6 . In Cobalt, the computational grid can be divided into group of cells, or zones, for parallel processing, where high performance and scalability can be achieved even on ten thousands of processors. Some available turbulence models in Cobalt are the Spalart-Allmaras (SA) model,¹² Spalart-Allmaras with Rotation Correction (SARC),¹³ and Delayed Detached-eddy simulation (DDES) with SARC.

Cobalt is based on an arbitrary Lagrangian-Eulerian formulation and hence allows all translational and rotational degrees of freedom. The code can simulate both free and specified six degree of freedom (6DoF) motions. The rigid motion is specified from a motion input file. For the rigid motion the location of a reference point on the aircraft is specified at each time step. In addition the rotation of the aircraft about this reference point is also defined using the rotation angles of yaw, pitch, and bank.

The Cobalt solver (version 7.0 used in this study) includes the option of an overset grid method that allows the independent translation and rotation of each grid around a fixed or moving hinge line. In this method, overlapping grids are generated individually, without the need to force grid points to be aligned with neighboring components.¹⁴ In Cobalt, the overlapping grids are treated as a single mesh using a grid-assembly process. This includes a hole-cutting procedure in overlapping regions and interpolation between overlapping grids. The translation and rotation of overset grids around the hinge line are input to the code using a grid control file. The hinge line is defined by a reference point and a vector combination. The rotations are right-handed and consist of angles in the order of pitch, yaw, and roll angle. These angles are calculated from the deflection angle of a control surface and the relative angles between the hinge line and grid coordinate axes.

E. CFD Calculation of Dynamic Derivatives

Static aerodynamic coefficients of Table 1 are directly calculated from static CFD simulations of the aircraft at given flight condition. However, a method is required to extract and separate damping derivatives from time-accurate CFD solutions. Pitch, yaw, and roll oscillations are often used to extract dynamic effects in terms of derivatives. The time-histories of aerodynamic coefficients undergoing these motions depend on the motion amplitude, mean angle, reduced frequency, and in particular the selected time-step. A linear regression method is used in this paper to determine TCR damping derivatives from forced oscillation motions in pitch, yaw, and roll directions. This method is briefly described.

During a forced-oscillation pitch, the lift and pitching moment can be written as:

$$\begin{aligned} C_L &= C_{L0} + C_{L\alpha}\alpha + (C_{L\dot{\alpha}} + C_{Lq}) \frac{qc}{2V} \\ C_m &= C_{m0} + C_{My\alpha}\alpha + (C_{m\dot{\alpha}} + C_{mq}) \frac{qc}{2V} \end{aligned} \quad (2)$$

where $(C_{L\dot{\alpha}} + C_{Lq})$ is pitch damping force (PDF) and $(C_{m\dot{\alpha}} + C_{mq})$ is pitch damping moment PDM. Likewise during a forced-oscillation in yaw:

$$\begin{aligned}
C_Y &= C_{Y_0} + C_{Y\beta}\beta + \left(C_{Y_r} - C_{Y\dot{\beta}}\right) \frac{rb}{2V} \\
C_{ROLL} &= C_{ROLL_0} + C_{ROLL\beta}\beta + \left(C_{ROLL_r} - C_{ROLL\dot{\beta}}\right) \frac{rb}{2V} \\
C_{YAW} &= C_{YAW_0} + C_{YAW\beta}\beta + \left(C_{YAW_r} - C_{YAW\dot{\beta}}\right) \frac{rb}{2V}
\end{aligned} \tag{3}$$

where the minus sign in combined terms means that a positive yaw rate will decrease the wing's side-slip angle. $\left(C_{ROLL_r} - C_{ROLL\dot{\beta}}\right)$ is named yaw damping moment1 (YDM1) in this paper and $\left(C_{YAW_r} - C_{YAW\dot{\beta}}\right)$ is yaw damping moment2 (YDM2). Finally, during a forced-oscillation in roll, the aerodynamic coefficients are found as:

$$\begin{aligned}
C_Y &= C_{Y_0} + C_{Y\beta}\beta + C_{Y_p} \frac{pb}{2V} \\
C_{ROLL} &= C_{ROLL_0} + C_{ROLL\beta}\beta + C_{ROLL_p} \frac{pb}{2V} \\
C_{YAW} &= C_{YAW_0} + C_{YAW\beta}\beta + C_{YAW_p} \frac{pb}{2V}
\end{aligned} \tag{4}$$

where $p(t) = \dot{\phi}(t)$ and $\phi(t)$ is the roll or bank angle at each time instant. C_{ROLL_p} and C_{YAW_p} are named RDM1 and RDM2, respectively. Note that the side-slip angle of $\beta(t)$ is related to the bank angle of $\phi(t)$ as:

$$\beta(t) = -\sin^{-1}(\sin\alpha \sin\phi(t)) \tag{5}$$

All above models are linear in structure; in general the function of y could be written in form of a linear mathematical model as:

$$y = \beta_0 + \beta_1 x_1 + \beta_2 x_2 + \dots + \beta_k x_k + \epsilon \tag{6}$$

where x_1, x_2, \dots, x_k are independent inputs; $\vec{\beta} = [\beta_0, \beta_1, \dots, \beta_k]$ is the vector of unknown coefficients and ϵ is the approximation error. Assuming there are n samples of function of y , define the vectors of $\vec{y} = [y_1, y_2, \dots, y_n]$ and $\vec{\epsilon} = [\epsilon_1, \epsilon_2, \dots, \epsilon_n]$. In this work \vec{y} contains CFD data from forced oscillation simulations and n is the number of time steps. Independent inputs of x_1, x_2, \dots, x_k are the variables used in Eqs. 2-4 (e.g. α, β, \dots). These variables are known at each time step of motion. The input matrix of X is then defined as:

$$\mathbf{X} = \begin{bmatrix} 1 & x_{11} & \cdots & x_{k1} \\ 1 & x_{12} & \cdots & x_{k2} \\ \vdots & \vdots & \ddots & \vdots \\ 1 & x_{1n} & \cdots & x_{kn} \end{bmatrix} \tag{7}$$

The sum of squared errors should be minimized; the squared error is:

$$S = \left(\vec{y} - X^T \vec{\beta}\right)^T \left(\vec{y} - X^T \vec{\beta}\right) \tag{8}$$

The unknown parameters can then be estimated as:

$$\vec{\beta} = (X X^T)^{-1} (X \vec{y}) \tag{9}$$

F. SDSA Stability and Control Analysis Code

The Simulation and Dynamic Stability Analysis (SDSA) code¹⁵ available in CEASIOM, performs stability analysis, 6DoF simulation, and flight control system design from generated aerodynamic models. For eigenvalues analysis, the nonlinear model of equations of motion is linearized by computing the Jacobian matrix at equilibrium (trim) point.¹⁵ The solution of eigenvalue problem has the general form of

$$\lambda = \xi + i\eta \quad (10)$$

where ξ and η are damping and frequency coefficients, respectively. The damping ratio and undamped frequency are estimated as:

$$\zeta_d = \frac{\xi}{\sqrt{\xi^2 + \eta^2}} \quad (11)$$

$$\omega_{nd} = \frac{\eta}{\sqrt{\xi^2 + \eta^2}} \quad (12)$$

The period is:

$$T = \frac{2\pi}{\eta} \quad (13)$$

III. Test Case

The TCR design concept, proposed by SAAB, is a conceptual design of a civil transport aircraft operating at transonic speeds. The design specifications are:

Payload: Nominal design for 200 passenger in economy class

Design Cruise Speed: $M_D = 0.97$ at an altitude at or above 37,000 ft.

Range: 5,500 nm, followed by 250 nm flight to an alternate airfield and 0.5 hour loiter time at an altitude of 1,500 ft.

Take-off and landing: Take-off distance of 8858 ft at an altitude of 2,000 ft, ISA+15 and maximum take-off weight. Landing distance of 6561 ft at an altitude of 2,000 ft, ISA and maximum landing weight with maximum payload and normal reserves.

Power plants: Two turbofans

The aircraft design is a mid-to-low winged canard configuration that has two wing mounted engines. The conventional aileron surfaces are located on the wing, and a rudder surface on the vertical tail. The canard is an all-movable surface. The canard exposed area is about 15 percent of the wing reference area. The wing sections has NACA 64A206 airfoil section with an outer sweep angle of 50 degrees. The canard has NACA 64A006 airfoil section with 53 degrees leading-edge sweep.

A CEASIOM-based model of the aircraft was generated and shown in Figure 1. Note that this is a simplified geometry of the aircraft and thus lacks the geometry refinements of final design. A CAD model of the TCR was created using CEASIOM-based geometry. This model is scaled 1:40 of the full aircraft for wind tunnel experiments and has not the engine, aileron, and rudder surfaces. Parameters for the wind tunnel experiment and our computational model are provided in Table 2.

The original TCR model has a canard positioned at 0.12 of total fuselage length and at the mid fuselage section. This is named “Design1” in this paper. A second design (named “Design2”) is considered as well that has canard positioned at 0.175 of total fuselage length and at a lower position than the original design. The CAD models of these designs were created in CEASIOM and shown in Figure 2. Full-geometry overset grids of the TCR designs (Design1 and Design2) were generated from these CADs. In these grids, a background viscous mesh was created around the fuselage, wing, and the tail. The canard viscous grids (right and left) were generated individually as well. The surface grids are shown in Figure 3. The canard grids are then overset to the background mesh as illustrated in Figure 4 (a). Right- and left-side canard grids have fringe boundary surfaces (FBSs) that transfer information between grids. The overset grid module in Cobalt then

Table 2. Specifications of the wind tunnel model of the TCR.

Parameter	Values
Wing area, S_w	0.3056 m^2
Canard area, S_c	0.045 m^2
Wing span, b_w	1.12 m
Canard span, b_c	0.3 m
Mean aerodynamic chord, c	0.2943 m
CG position from the aircraft nose, x_{CG}	0.87475 m
Total fuselage length	1.597 m
Fuselage Diameter	0.925 m

performs an automatic hole cutting by interpolating FBS in each grid. The hole cutting process can be seen in Figures 4 (b)-(c). The assembled grids for canard deflections of 10° and -30° are shown in Figure 4 as well. Each canard (minor) grid contains about six million cells while the background grid has about 60 million cells. The assembled grid has about 70 million cells.

Note that a grid assembly approach in the Cobalt code requires some gaps between the canard and the body. This gap is shown in Figure 5. This gap was deemed acceptable by Ghoreyshi *et al.*⁵ by comparison of overset and single (without any gap) grid predictions.

The TCR wind-tunnel model was built with a geometric scaling factor of 1:40 of the actual size to fit the size requirements of the TsAGI subsonic wind tunnel. This wind tunnel has an open jet working section of the continuous type with an elliptical cross section of $4.0 \times 2.33m$.¹⁶ The wind tunnel can operate at velocities up to 80 m/s and Reynolds numbers up to 5.5 million based on a reference length of 0.2943m. For the dynamic tests, the model was mounted on a platform driven by actuators. The model center of gravity was located along the fuselage center line at 54.78% of the total length from the foremost point. The moment reference point and the center of oscillatory motion coincide with this point.

The normal and lateral forces and the moment coefficients from static and large amplitude pitch oscillations were measured. The mean values, in-phase and out-of-phase components of the force and moment coefficients were also measured from the rotary and oscillatory motions. All aerodynamic coefficients are given in the body axis system.

All experiments were run at a free-stream speed of 40 m/s, which corresponds to a sea level Mach number of 0.117, and a Reynolds number of 0.778 million based on the mean aerodynamic chord of the wind tunnel model. This experimental data can be obtained from the SimSAC project website (<http://www.ceasium.com>) and are used in this work to validate the overset grid approach and the Cobalt CFD solver used at the U.S. Air Force Academy (USFA).

IV. Results and Discussion

Aerodynamic look-up tables (see Table 1) are filled with TCR wind tunnel experiments, Cobalt simulations, and Tornado code calculations. The wind tunnel data are only available at low subsonic speeds. The potential flow solver calculations do not change with Mach number as well. Therefore, all tables entities corresponding to a Mach number of 0.9 are filled with low speed aerodynamic data. Note that the CEASIOM code needs a minimum of two values for each state and control parameter in the tables. In order to have a fair comparison between flight dynamic results predicted from wind tunnel data, Tornado code, and Cobalt simulations, it was decided to run CFD simulations at low subsonic speeds as well. Therefore, in all Cobalt simulations, the free-stream velocity is 40m/s and the Reynolds number corresponds to 0.778 million based on the mean aerodynamic chord to match wind tunnel conditions. All Cobalt simulations were run on the Department of Defense High Performance Computing Modernization Program (HPCMP).

The SDSA codes needs aerodynamic data for all longitudinal and lateral control surfacens. However, the aileron and rudder surfaces are not available in the wind tunnel experiments and CFD simulations. Therefore, aileron and rudder aerodynamic predictions from Tornado code were used to fill wind tunnel and CFD aerodynamic tables. In addition, wind tunnel experiments have no drag data. CFD drag predictions

were used instead in wind tunnel look-up tables.

For comparison plots, all aerodynamic coefficients(except drag) are presented in the body axis system. For aerodynamic tables, however, coefficients were given in the wind axis. In static CFD simulations, a first order accuracy in time with a CFL number of one million and one Newton sub-iteration was used. In dynamic simulations, second order accuracy was used with a non-dimensional time step of 0.01 and five Newton sub-iterations. Turbulence model used in all simulations is SARC which Ghoreyshi *et al.*⁵ found reasonable to predict the vortical flows formed over TCR configuration.

A. Aerodynamic Predictions

Aerodynamic tables have 576 entities for all combinations of flight conditions considered in this work. A brute-force approach was used to fill the tables. Tornado calculations took less than an hour to fill whole table. Each entity in the table corresponding to a static condition, took about 2,680 CPU hours to complete by CFD solver. Dynamic derivatives at each angle of attack took about 10,000 CPU hours as well.

Figure 6 shows Tornado panels for the TCR Design-1. The model has the wing, canard, and vertical tail but not the fuselage. The canard is all movable. Figure 7, for example, shows TCR tornado solutions at ten degrees angle of attack and at zero and ten degrees canard deflections. The pressure differences between lower and upper surfaces are shown in this Figure. This figure shows that a positive canard deselection (trailing edge down) produces a negative pressure region around the leading edge (hinge line).

Longitudinal aerodynamic predictions of TCR-Design1 using CFD and Tornado code are shown in Figure 8 and compared with wind tunnel measurements. Figure 8 shows that CFD data closely match with experiments at almost all angles of attack. TCR-Design1 shows no sign of stall in the range of angles of attack presented. However, the aerodynamic data are highly nonlinear in particular at moderate to high angles of attack. For example, both CFD and experiment show a negative slope pitching moment at small angles of attack. At about eight to ten degrees angle of attack, the pitching moment slope becomes zero and even positive. For a zero canard deflection, the pitching moment slope again becomes negative about 20 degrees angle of attack. Figure 8 shows that a positive canard deflection increases normal force and pitching moment. The drag will also become higher than non-deflected canard at high angles of attack.

Figure 8 shows that Tornado code predictions are very different from wind tunnel measurements and CFD predictions. The pitching moment slope is less negative probably due to lack of fuselage effects. The slopes are nearly linear with angle of attack as well. Drag data are not presented in the figure, they underestimate (about one order of magnitude) CFD drag values.

Additionally, Figure 9 compares lateral force and moment coefficients predicted at -6 and 6 degrees sideslip angles with those measured in the wind tunnel. Overall, a good match between CFD and wind tunnel measurement is found. Tornado data are close to CFD data at small angles of attack but not at high angles. Figure 9 shows that TCR rolling moment is a nonlinear function of angle of attack even at small angles. The rolling moment slope increases with angle of attack up to six degrees, which it becomes nearly constant and then falls at higher angles. Side-force and yawing movement slope suddenly fall above ten degrees angle of attack as well.

Predicted damping derivatives are presented in Figure 10 and compared with experiments. These derivatives were estimated from forced oscillation motions in pitch, yaw, and roll directions. The mean angle of attack varies from zero to ten degrees. The motion amplitude is 0.5 degree and motion frequency is 1Hz. Figure 10 shows that CFD data match better with experiments than Tornado code. Derivatives calculated by Tornado code are linear function of angle of attack. Some derivatives have opposite signs than those measured in the wind tunnel. These discrepancies are mainly due to not modeling the fuselage and the code inability to predict vortical flows over TCR configuration.

Some flow features of TCR-Design1 are presented in Figure 12 in which vorticity isosurfaces are colored by pressure coefficient. Figure 12 shows tip vortices formed at six degrees angle of attack. At $\alpha = 8^\circ$, a vortex is formed over the wing, however, the vortex starting point is not at the wing apex. This vortex induces negative pressures over the surface and causes the lift to increase. At higher angles of attack, the vortex starting point moves toward the wing apex which causes a positive increment in the pitching moment. At $\alpha = 10^\circ$, the vortex starting point is at the wing apex. The canard vortex can be seen at this angle. Further increase in the angle of attack does not move the vortex starting point, but vortices become stronger and larger in size. At about $\alpha = 20^\circ$, the canard vortex lifts up from the surface and the canard lift suddenly drops causing more changes in the pitching moment slopes.

Static aerodynamics of both TCR designs are compared in Figure 12. The moment reference point is the same in both simulations. The results show that both designs have very similar coefficients at small angles of attack, except pitching and rolling moments that are slightly different due to different moment arms about the moment reference point. At higher angles, large differences can be seen between these designs. For example, Design-2 has bigger lateral force and moment coefficients up to 22 degrees angle of attack. The pitching moment slopes are different as well. In addition, damping derivatives of both TCR designs are compared in Figure 13 which shows that both canard positions produce close damping derivatives in particular at high angles of attack. Finally, some of the flow features of TCR-Design2 are shown in Figure 14. The flow structures are similar to those found in Design-1, except that the aft-positioned canard has stronger canard vortices.

B. Stability and Control Predictions

Aerodynamic tables of TCR-Design1 generated by wind tunnel, CFD simulations, and Tornado code were input to SDSA code to investigate the vehicle stability and handling qualities. The aircraft altitude was set at 8,000 m and speed was varied from 100 to 300 m/s. Note that these flight conditions correspond to much higher Mach numbers than the one used in generating aerodynamic models. Though, the aircraft can be trimmed using Tornado-generated tables, the SDSA predicted no trim states for the aircraft for speeds below 200 m/s using wind tunnel and CFD tables. Figure 15 shows required angle of attack and canard deflection to trim the aircraft at 8,000m and different speeds. Figure shows that required angle of attack increases at small speeds. At some angle of attack, the pitching moment slopes become zero or positive and therefore no trim state can be obtained. However, Tornado pitching moment slope are negative for considered angles of attack and it still predicts a trim point at wider range of air speeds.

In more detail, Figure 15 shows that predictions from a Tornado code require larger angles of attack and less canard deflections to trim aircraft compared with wind tunnel and CFD predictions. All models predict satisfactory phugoid stability performance, however, Tornado tables predict much larger damping ratios than experimental and CFD data.

Figure 16 also compares roll stability results calculated in the SDSA code using different aerodynamic tables. The results are similar and the same range for all three aerodynamic sources, however, wind tunnel and CFD show more nonlinear trends than Tornado predictions.

Finally, Figures 17 and 18 compare flight dynamics predictions from different TCR designs. Note that in Design2, the center of gravity was shifted backward about 0.2m (in actual aircraft size). The results show that considering the center of gravity changes, Design2 requires slightly less canard deflections than Design1 to trim the aircraft. The aerodynamic predictions of these configuration are mainly different at high angles of attack. However, the aircraft cannot be trimmed at higher angles due the break present in pitching moment, Figures 17 and 18 do not show major changes in aircraft stability and control at these canard positions.

V. Conclusions

This work presented the canard wing interference effects on the flight characteristics of a civilian transonic cruiser. The low speed aerodynamic characteristics of the TCR are available from the SimSAC project and were used in this work to validate CFD predictions. All tests were run at a free-stream velocity of 40 m/s, which corresponds to a sea level Mach number of 0.117, and a Reynolds number of 0.778 million based on the mean aerodynamic chord of the wind tunnel model.

An overset grid method was used to simulate canard deflections available in the experiments, however, a gap region is required between the canard (overset mesh) and the aircraft (background mesh) to allow the mesh assembly. Overall, a good agreement was found between CFD and experiments for most cases. Both CFD and experiment show a negative slope pitching moment at small angles of attack. Two breaks present in the pitching moment plots as well, one about eight to ten degrees angle of attack because of moving the wing vortex starting point and the second one about 20 degrees angle of attack due to lifting up the canard surface. Tornado code, however, predicts a less negative pitching moment slope and cannot predict the breaks seen in the pitch moments.

The predicted dynamic damping derivatives from the potential solver do not match the experimental data due to not having the fuselage section in the model and inability of the solver to predict vortical flows over the vehicle. The aerodynamic models are then used in a stability and control analysis code to investigate

the trim setting and handling quality of different canard designs. Overall, computed aerodynamics from the high-fidelity solver leads to similar flight dynamics results obtained from experimental data. The results show that positioning the canard surface of this vehicle closer to the wing requires less canard deflection and thrust force to trim the aircraft. These results confirm that computational fluid dynamics is a promising tool in design and flight dynamics investigation of aircraft with no historical data.

VI. Acknowledgements

This work was performed under Cooperative Agreement FA7000-16-2-0003 with the US Air Force Academy, with financial support coming from the US DoD High Performance Computing Modernization Program. Mehdi Ghoreyshi is supported by USAFA under contract FA70001320018; this financial support is gratefully acknowledged. Acknowledgements are expressed to the Department of Defense High Performance Computing Modernization Program (HPCMP), ERDC for providing computer time.

References

- ¹Eliasson, P., V. J., Da Ronch, A., Zhang, M., and Rizzi, A., "Virtual Aircraft Design and Control of TransCruiser - A Canard Configuration," AIAA Paper 2010-4366, July 2010.
- ²Ghoreyshi, M., Badcock, K. J., and Woodgate, M. A., "Accelerating the Numerical Generation of Aerodynamic Models for Flight Simulation," *Journal of Aircraft*, Vol. 46, No. 3, 2009, pp. 972-980.
- ³Ghoreyshi, M. and Cummings, R., "From Spreadsheets to Simulation-Based Aircraft Conceptual Design," *Applied Physics Research*, Vol. 6, No. 3, 2014, pp. 64-80.
- ⁴Von Kaenel, R., Rizzi, A., Ooppelstrup, J., Grabowski, T., Ghoreyshi, M., Cavagna, L., and Bérard, A., "CEASIOM: Simulating Stability & Control with CFD/CSM in Aircraft Conceptual Design," 26th International Congress of the Aeronautical Sciences, ICAS, 14 - 19 September 2008, Anchorage, Alaska, USA.
- ⁵Ghoreyshi, M., Korkis-Kanaan, R., Jirasek, A., Cummings, R., and Lofthouse, A., "Simulation Validation of Static and Forced Motion Flow Physics of a Canard Configured TransCruiser," *Aerospace Science and Technology*, Vol. 48, 2016, pp. 158-177.
- ⁶Williams, J. E. and Vukelich, S. R., "The USAF Stability and Control Digital DATCOM," McDonnell Douglas Astronautics Company - St Louis Division, St Louis, Missouri 63166, 1979, AFFDL-TR-79-3032.
- ⁷Rizzi, A., Eliasson, P., McFarlane, C., Goetzendorf-Grabowski, T., and Vos, J., "Virtual Aircraft Design and Control of TransCruiser - A Canard Configuration," AIAA Paper 2010-8245, August 2010.
- ⁸Melin, T., "TORNADO: a Vortex-Lattice MATLAB Implementation for Linear Aerodynamic Wing Applications," Master Thesis, Royal Institute of Technology (KTH), Department of Aeronautics, Sweden, December, 2000.
- ⁹Strang, W. Z., Tomaro, R. F., and Grismer, M. J., "The Defining Methods of Cobalt: A Parallel, Implicit, Unstructured Euler/Navier-Stokes Flow Solver," AIAA Paper 1999-0786, 1999.
- ¹⁰Gottlieb, J. J. and Groth, C. P. T., "Assessment of Riemann Solvers For Unsteady One-dimensional Inviscid Flows of Perfect Gasses," *Journal of Computational Physics*, Vol. 78, No. 2, 1988, pp. 437-458.
- ¹¹Tomaro, R. F., Strang, W. Z., and Sankar, L. N., "An Implicit Algorithm For Solving Time Dependent Flows on Unstructured Grids," AIAA Paper 1997-0333, 1997.
- ¹²Spalart, P. R. and Allmaras, S. R., "A One Equation Turbulence Model for Aerodynamic Flows," AIAA Paper 1992-0439, January 1992.
- ¹³Spalart, P. R. and Shur, M. L., "On the Sensitization of Turbulence Models to Rotation and Curvature," *Aerospace Science and Technology*, Vol. 1, 1997, pp. 297-302.
- ¹⁴Tuncer, I. H., Gulcat, U., Emerson, D. R., and Matsuno, K., *Parallel Computational Fluid Dynamics 2007*, Springer-Verlag, Germany, 2009.
- ¹⁵Goetzendorf-Grabowski, T., Mieszalski, D., and Marcinkiewicz, E., "Stability Analysis in Conceptual Design Using SDSA Tool," AIAA Paper 2010-8242, August 2010.
- ¹⁶Khrabrov, A., Kolinko, K., Zhuk, A., and Grishin, I., "Wind Tunnel Test Report," SimSAC Technical Report, October 2009.

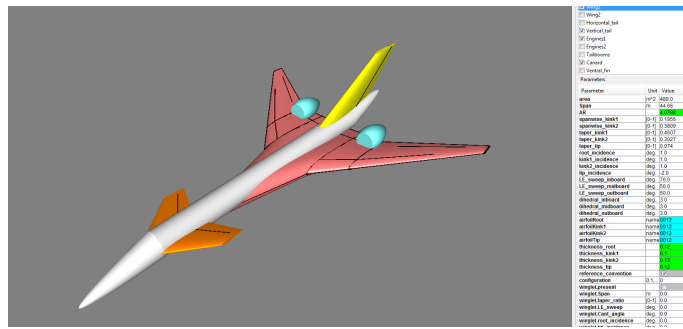


Figure 1. TCR model in the CEASIOM code.

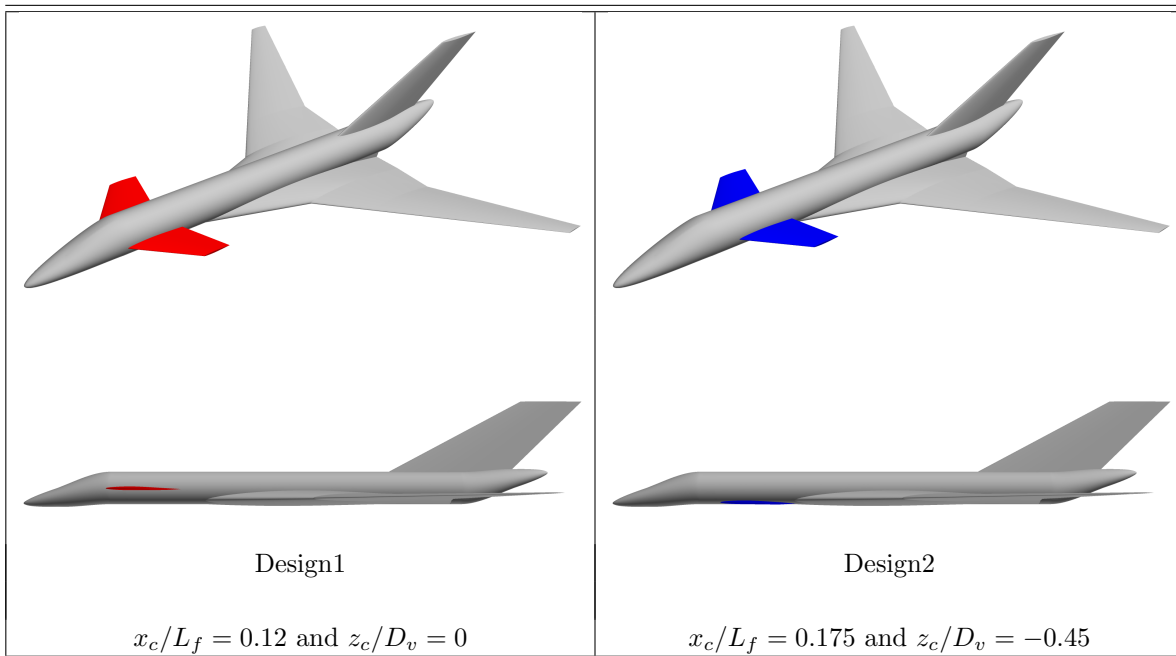
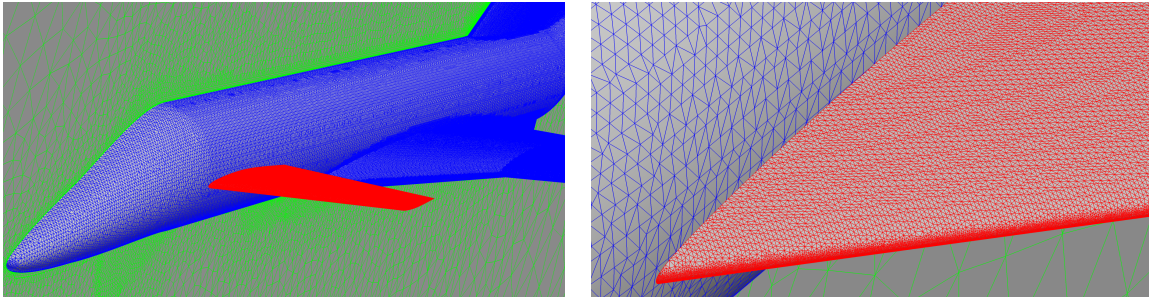


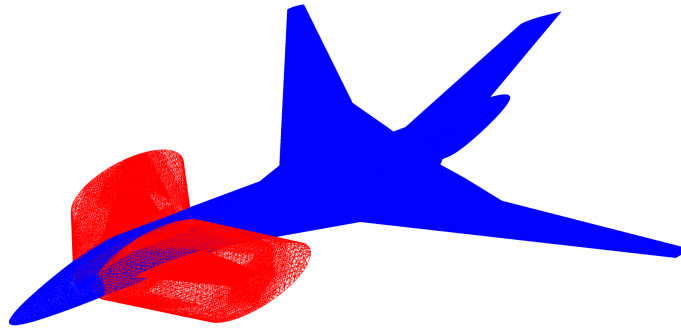
Figure 2. TCR designs with different canard positions.



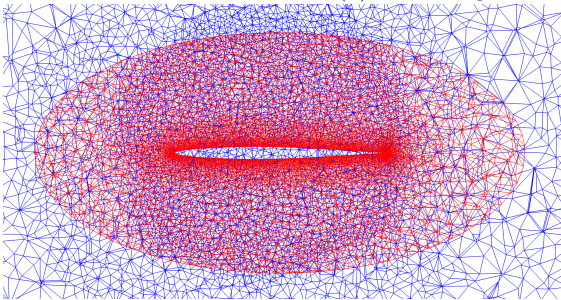
(a) Surface grid

(b) Canard surface grid

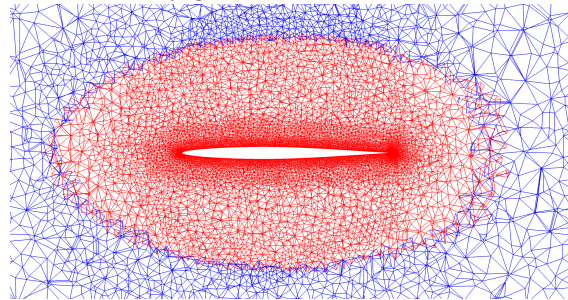
Figure 3. TCR Design1 surface grid.



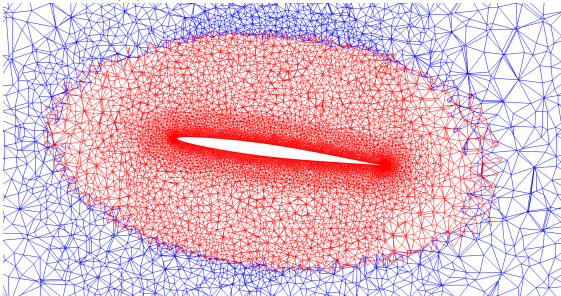
(a) Canard grids overset to the body grid



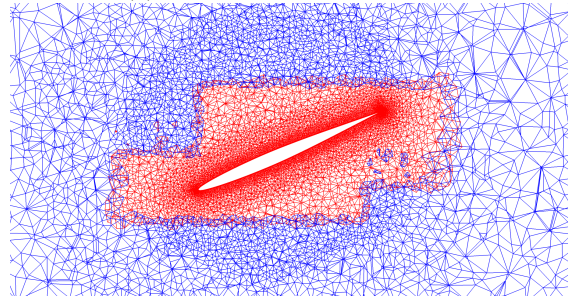
(b) Grids not assembled grids



(c) Assembled grid - $\phi_c = 0^\circ$



(d) Assembled grid - $\phi_c = 10^\circ$



(e) Assembled grid - $\phi_c = -30^\circ$

Figure 4. Illustration of the overset grid approach used to model canard deflections.

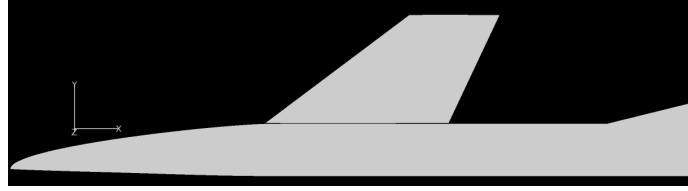


Figure 5. Illustration of the gap present between canard and fuselage.

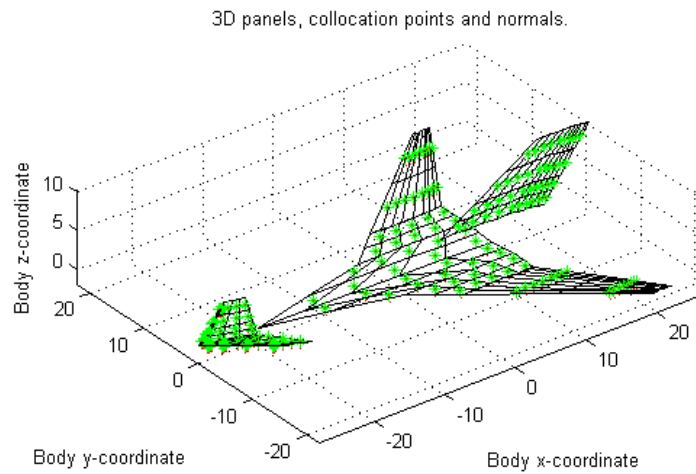


Figure 6. TCR Design1 model for use in potential flow solver.

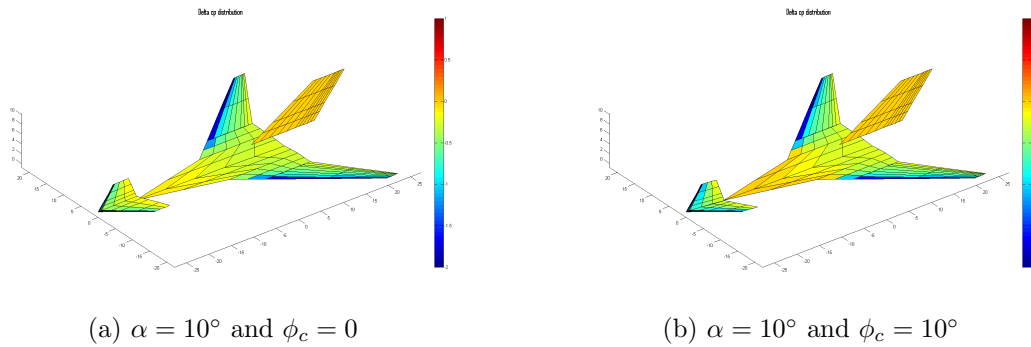
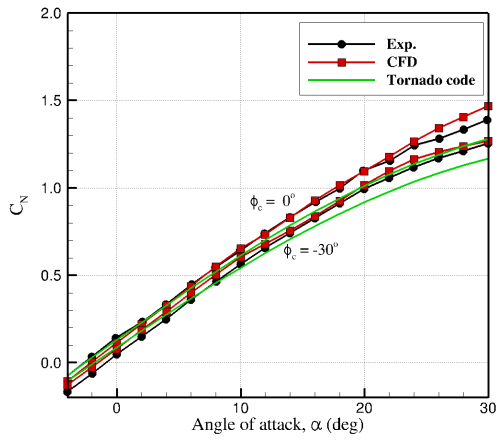
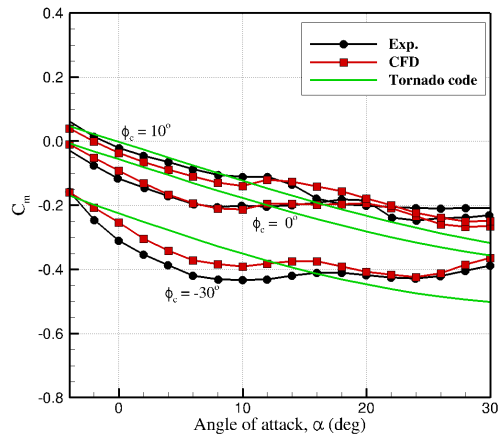


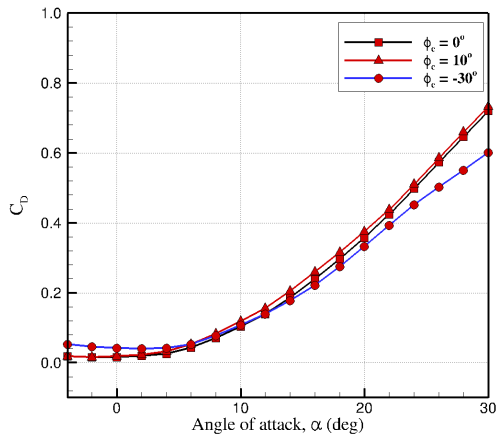
Figure 7. Potential flow solver solutions at ten degrees angle of attack and Mach number of 0.1.



(a) Normal force coefficient

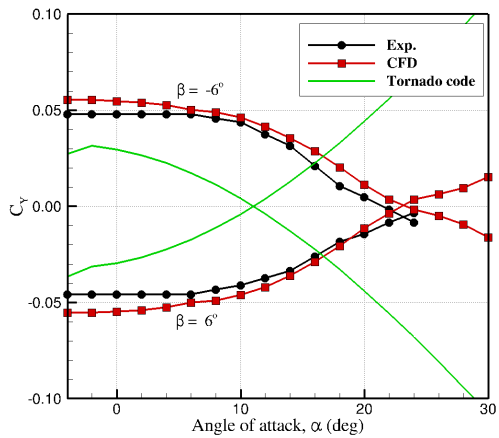


(b) Pitching moment coefficient

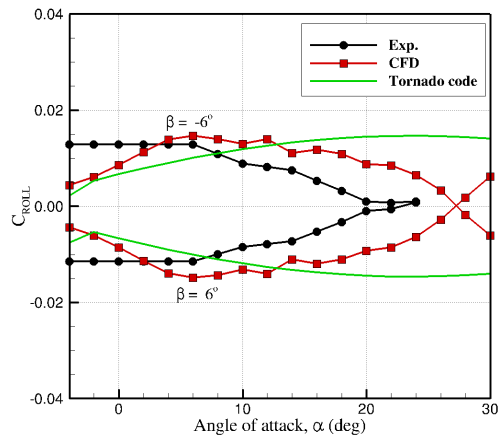


(c) Drag coefficient

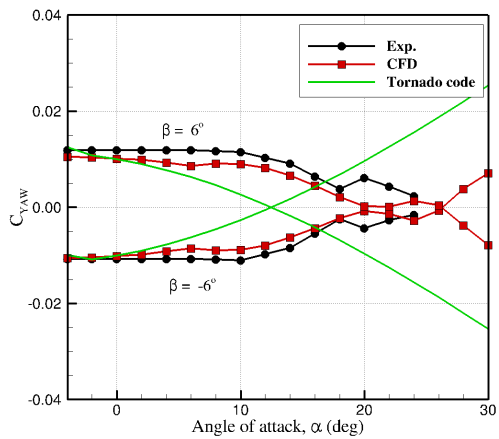
Figure 8. Comparison of TCR Design1 static longitudinal forces/moments with experiments. In (c) only CFD data are shown.



(a) Side force coefficient

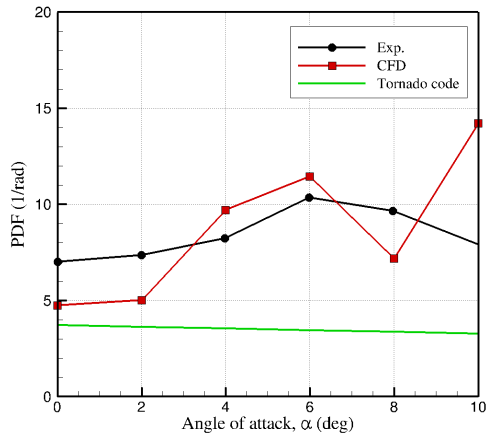


(b) Rolling moment coefficient

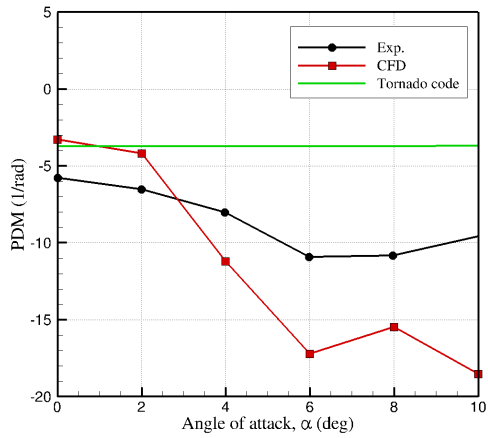


(c) Yawing moment coefficient

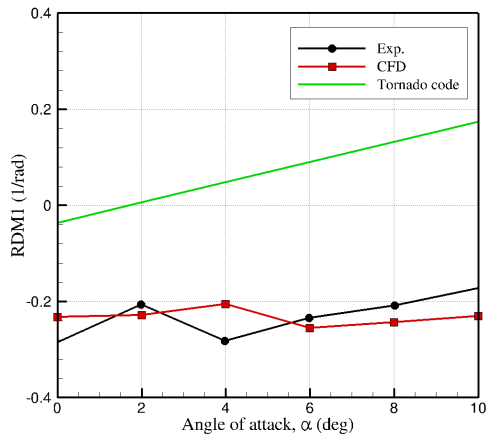
Figure 9. Comparison of TCR Design1 static lateral forces/moments with experiments.



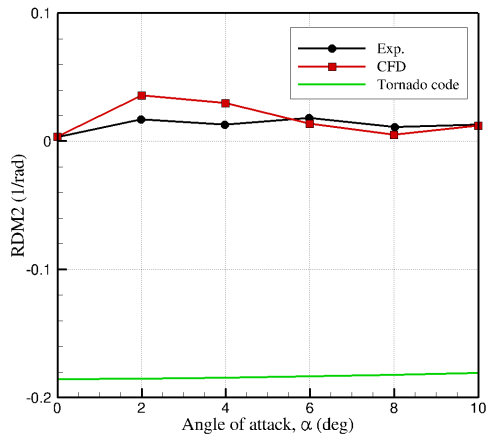
(a) Pitch damping force



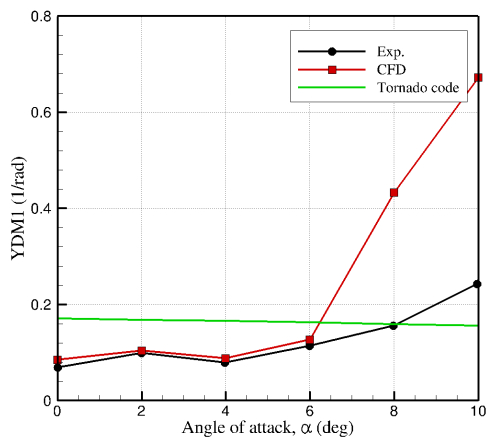
(b) Pitch damping moment



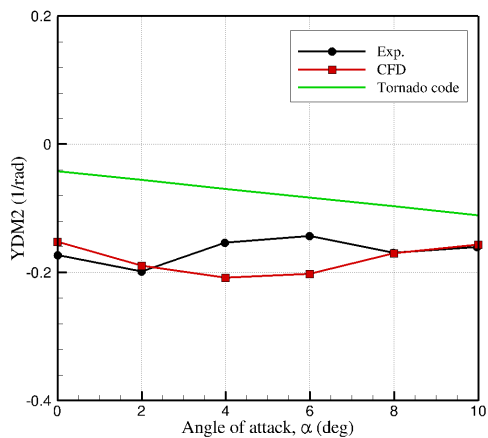
(c) Roll damping moment (roll moment)



(d) Roll damping moment (yaw moment)



(e) Yaw damping moment (roll moment)



(f) Yaw damping moment (yaw moment)

Figure 10. Comparison of TCR Design1 dynamic damping forces and moments with experiments.

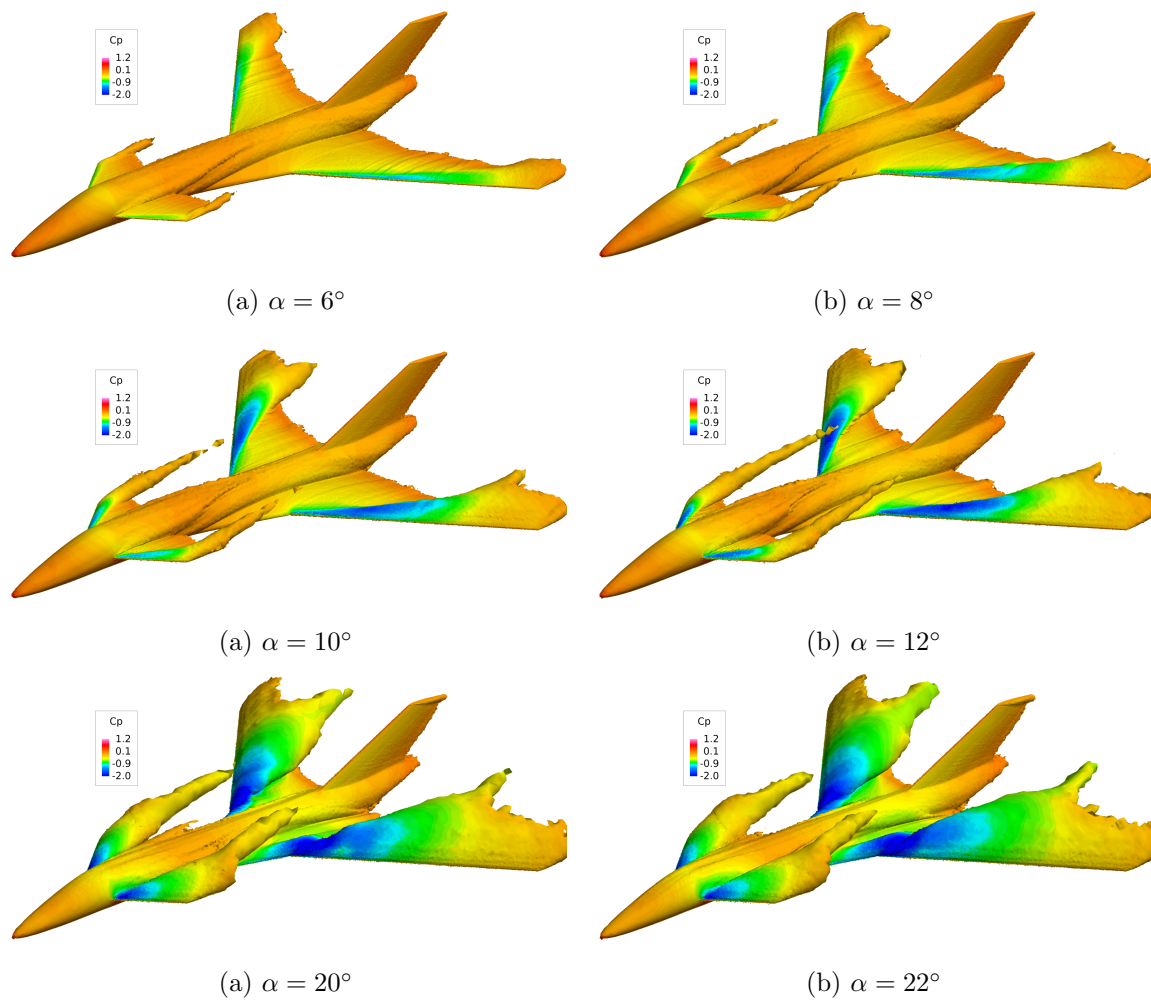
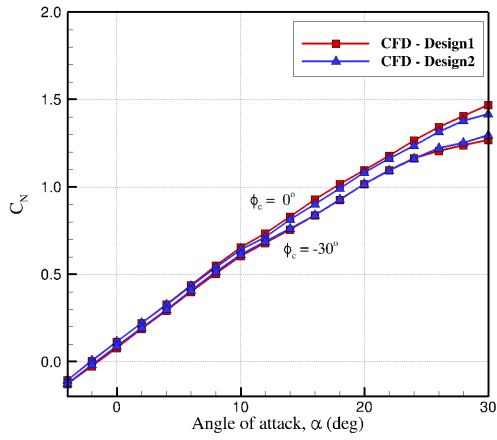
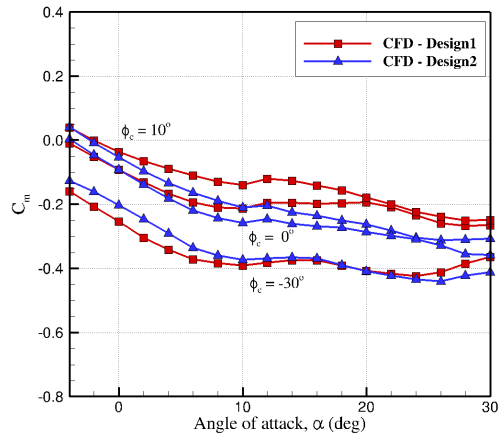


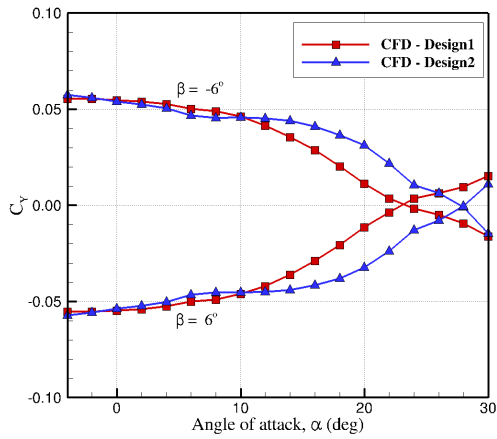
Figure 11. Flow solutions of TCR Design1 with $\phi_c = 0^\circ$. Vorticity isosurfaces are colored by pressure coefficient, C_p .



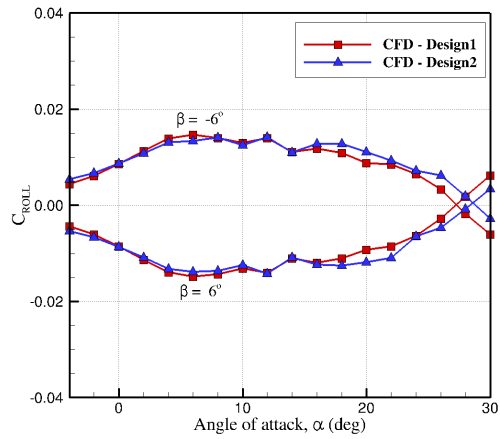
(a) Normal force coefficient



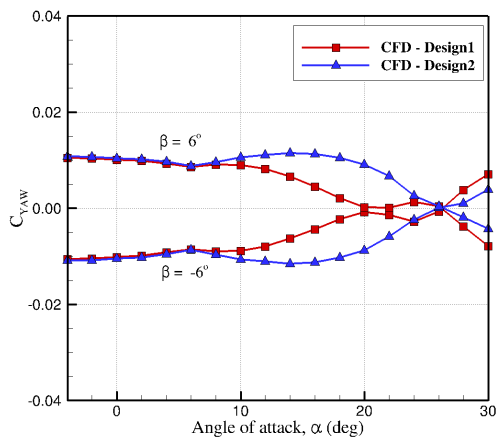
(b) Pitching moment coefficient



(c) Side force coefficient

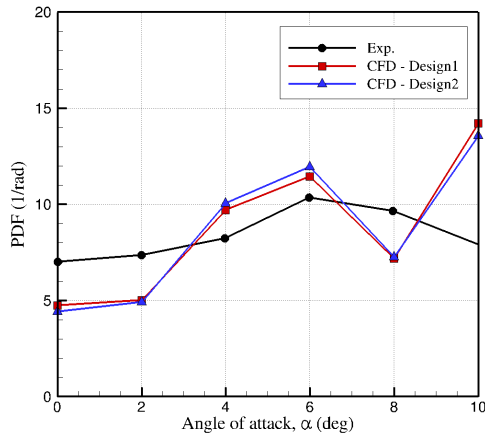


(d) Rolling moment coefficient

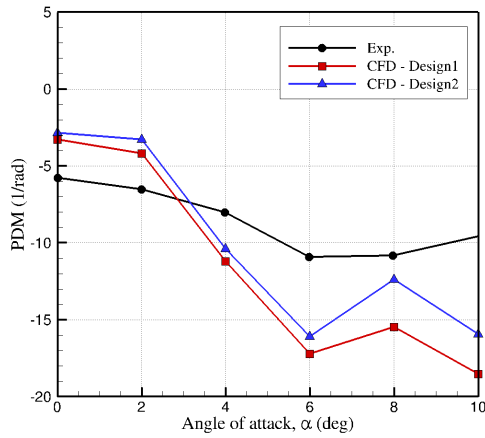


(e) Yawing moment coefficient

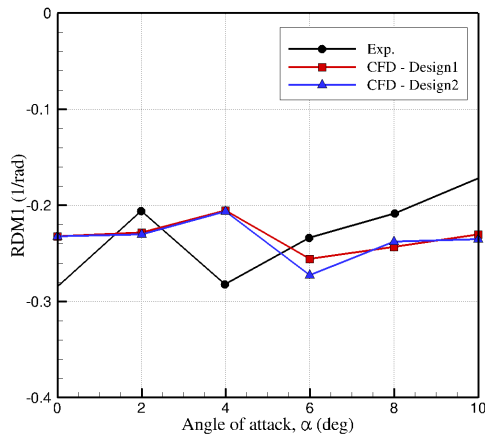
Figure 12. Comparison of TCR Design1 and Design2 static aerodynamic data.



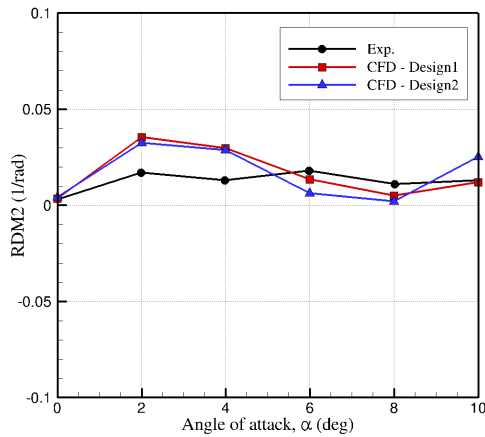
(a) Pitch damping force



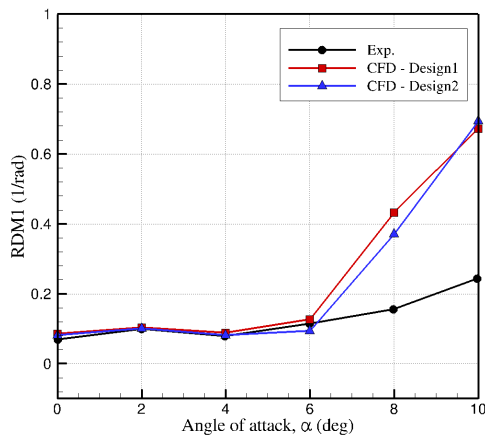
(b) Pitch damping moment



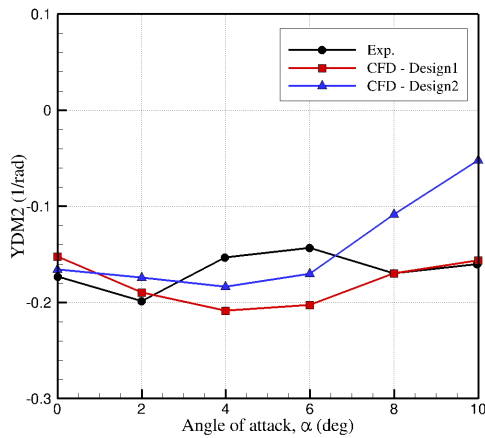
(c) Roll damping moment (roll moment)



(d) Roll damping moment (yaw moment)



(e) Yaw damping moment (roll moment)



(f) Yaw damping moment (yaw moment)

Figure 13. Comparison of TCR Design1 and Design2 dynamic aerodynamic data.

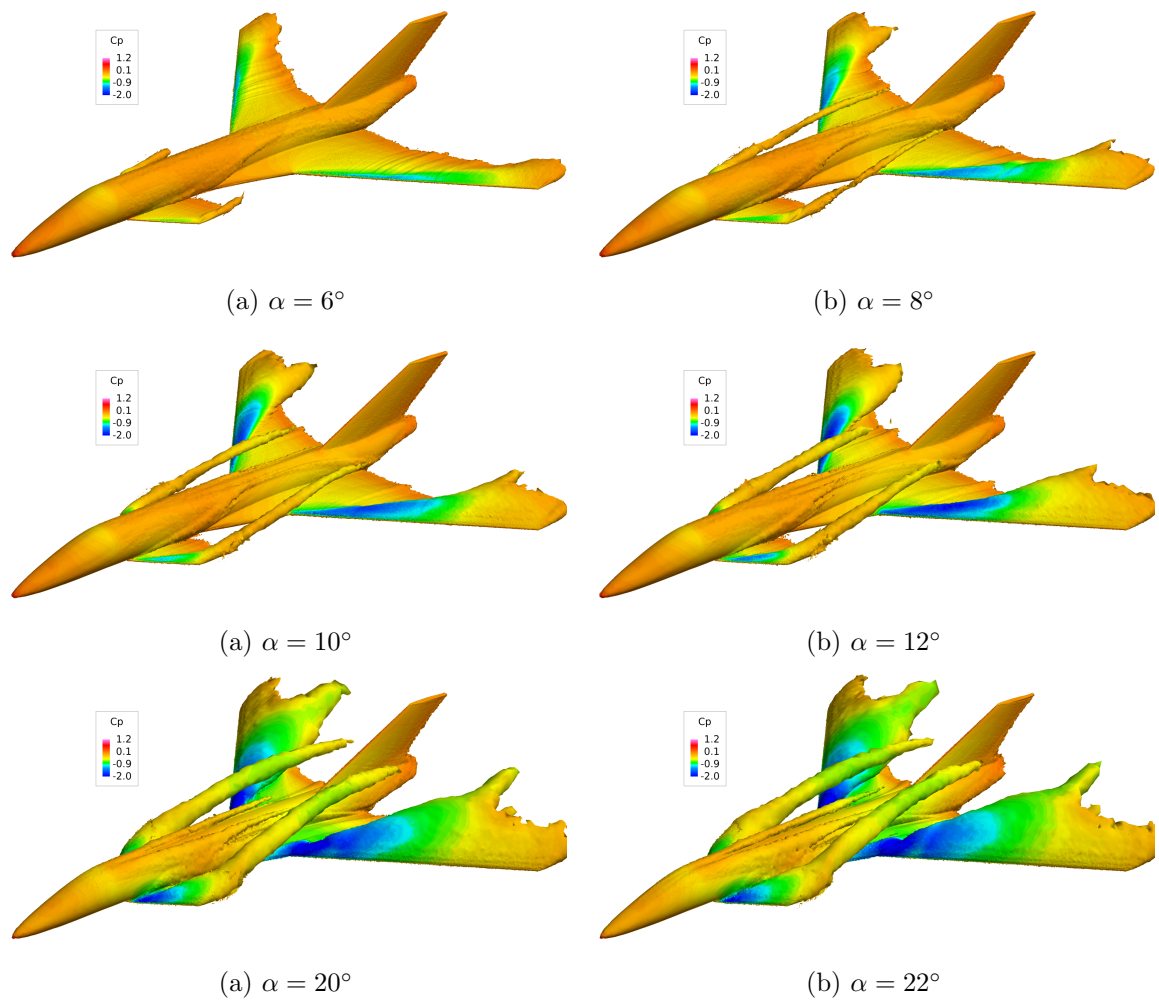
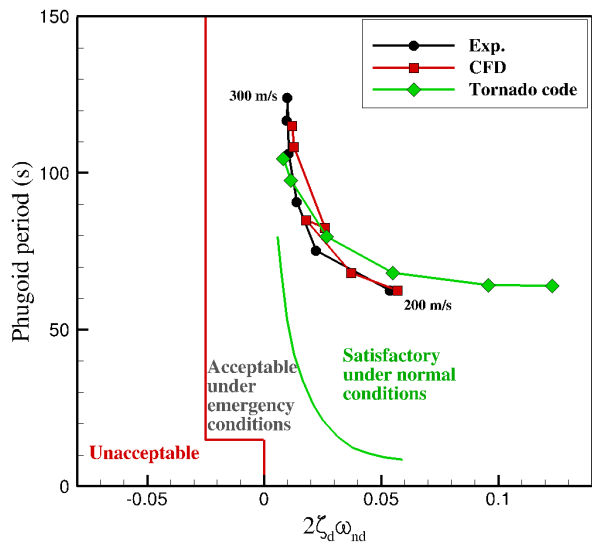
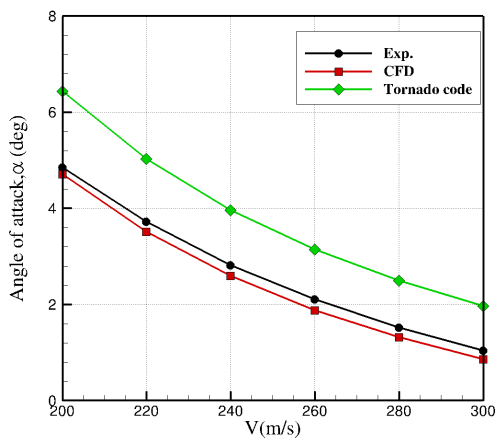


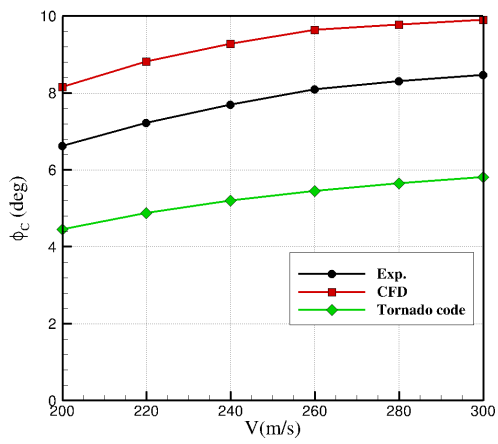
Figure 14. Flow solutions of TCR Design3 with $\phi_c = 0^\circ$. Vorticity isosurfaces are colored by pressure coefficient, C_p .



(a) ICAO stability criteria for phugoid

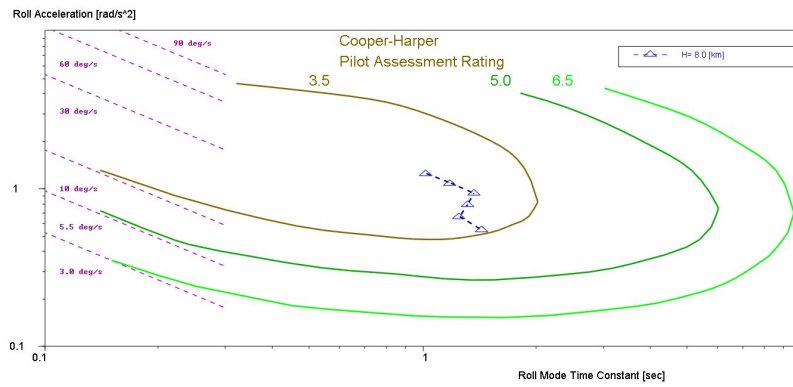


(b) Trim angle of attack

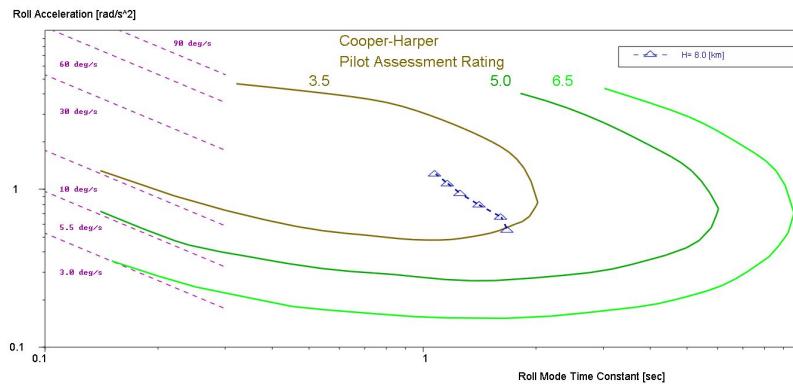


(c) Trim canard deflection

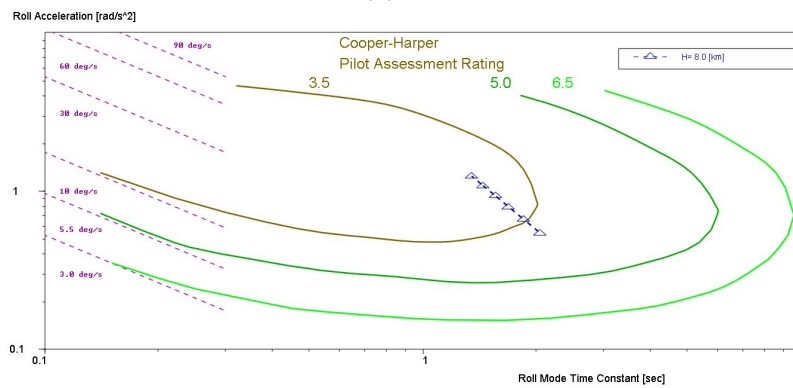
Figure 15. Design1 longitudinal stability results at 8,000m.



(a) Experimental data

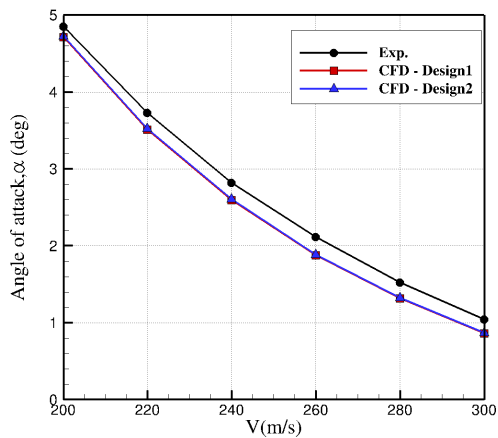


(b) CFD

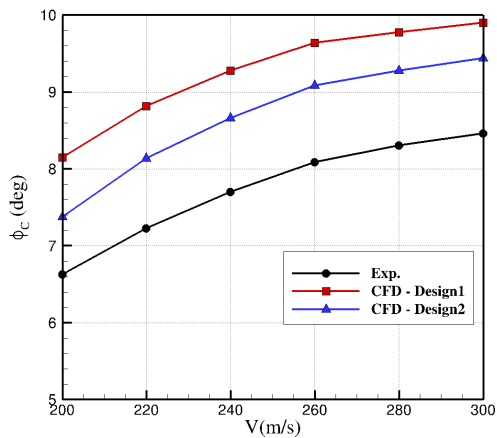


(c) Tornado code

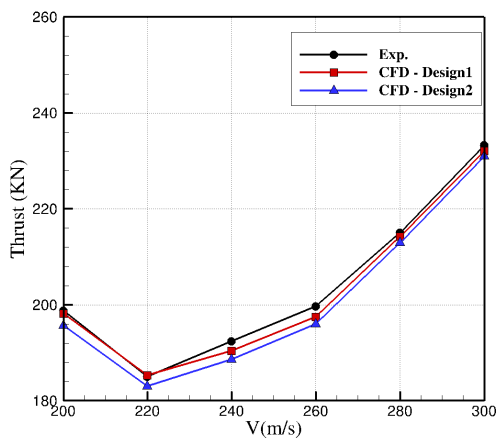
Figure 16. Design1 roll stability results at 8,000m.



(a) Trim angle of attack

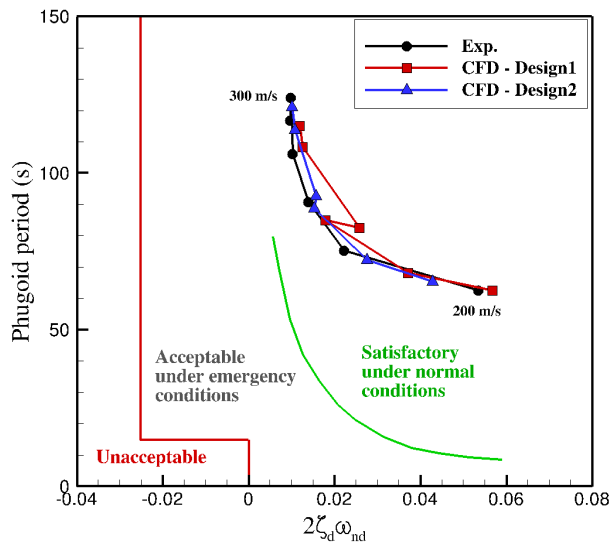


(b) Trim canard deflection

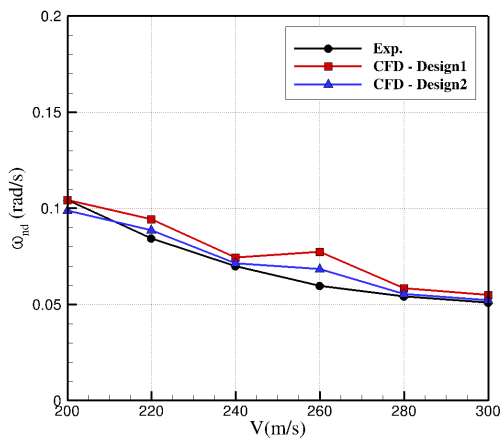


(c) Required thrust

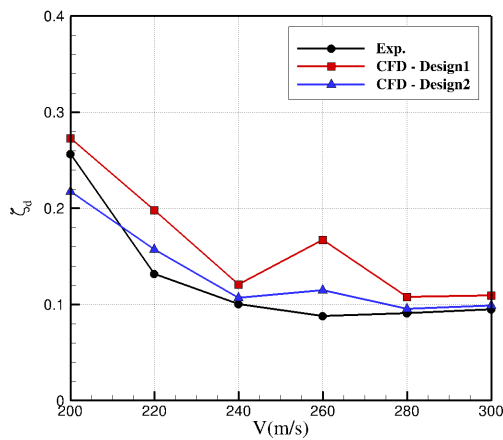
Figure 17. Trim results at 8,000m.



(a) ICAO stability criteria for phugoid



(b) Phugoid undamped natural frequency



(c) Phugoid damping ratio

Figure 18. Longitudinal stability results at 8,000m.